Self-induced Berry flux and spontaneous non-equilibrium magnetism

Mark S. Rudner[1*] and Justin C. W. Song[2,3†]
[1] *Center for Quantum Devices and Niels Bohr International Academy, Niels Bohr Institute, University of Copenhagen, 2100 Copenhagen, Denmark*
[2] *Division of Physics and Applied Physics, Nanyang Technological University, Singapore 637371 and*
[3] *Institute of High Performance Computing, Agency for Science, Technology, and Research, Singapore 138632*

When a physical system is governed by statistical or dynamical equations possessing certain symmetries, its stationary states can be classified into phases according to which of those symmetries are preserved, and which are broken [1, 2]. Near equilibrium, the properties of the system's collective excitations reflect the symmetries of the underlying phase and thereby provide means for detecting these phases [3, 4]. Here we show that, in driven systems, the collective modes may take on a separate life, exhibiting their own spontaneous symmetry breaking phenomena independent of the underlying equilibrium phase. We illustrate this principle by demonstrating a new mechanism through which an interacting system subjected to a time-reversal symmetric driving field can spontaneously magnetize. Here, the strong internal ac fields of a metal driven close to its plasmonic collective mode resonance [5, 6] enable *Berryogenesis*: the spontaneous generation of a self-induced Bloch band Berry flux. The self-induced Berry flux supports and is sustained by a circulating plasmonic motion, which may arise even for a *linearly polarized* driving field. This non-equilibrium phase transition occurs above a critical driving amplitude and may be of either continuous or discontinuous type. Berryogenesis can occur in a wide variety of multiband metals with high quality plasmons, as available in present-day graphene devices [7–9].

Note: *This is a repository archive version required by the funding agency publication policy. The article was published as Nature Physics 15, 1017-1021 (2019) with doi: 10.1038/s41567-019-0578-5. The journal published article can be found at https://www.nature.com/articles/s41567-019-0578-5.*

Interacting many-body systems may exhibit collective modes of excitation whose emergent properties are unlike those of the system's constituent particles. Importantly, such modes may host strong *internal fields* associated with the restoring force underlying the system's collective oscillations. For example, plasmons have recently gained wide attention for their ability to resonantly enhance applied electric fields by many orders of magnitude [5, 6].

Here we propose that interesting new collective mode phases may arise due to *feedback* in which a system's internal fields modify its microscopic properties, in turn altering its response to the driving field. Time-dependent driving by laser or microwave fields has recently emerged as a powerful tool for dynamically controlling the non-equilibrium properties of quantum matter [10–24]. As we discuss here, such fields provide the means to access non-equilibrium spontaneous symmetry breaking associated with novel collective mode phase transitions.

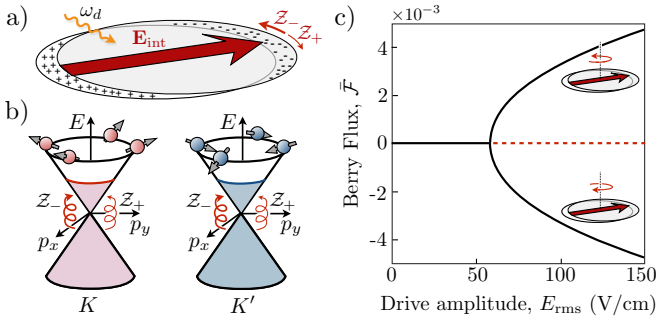

FIG. 1: *Berryogenesis*: Spontaneous generation of Berry flux in a time-reversal-invariant driven system. a) When excited, the dipole mode of a metallic disk hosts an internal electric field, $\mathbf{E}_{\rm int}(t)$, which oscillates at the drive angular frequency, ω_d. The corresponding motion is decomposed into right and left circulating amplitudes, $\mathcal{Z}_+$ and $\mathcal{Z}_-$, respectively. b) An off-resonant ac electric field dresses the electronic Bloch functions, yielding a finite Berry flux through the Fermi sea. In this way, ac *internal fields* may dynamically alter the system's electronic properties, giving rise to feedback. c) Stability diagram, with stable (unstable) solutions of Eq. (5) indicated by black solid (red dashed) lines. For small amplitudes of a linearly polarized drive, the response is linearly polarized ($\bar{\mathcal{F}} = 0$). Above threshold, the linearly polarized solution becomes unstable and the system spontaneously develops a right- or left- handed circulation. Parameters: $E_F = 160$ meV, $\hbar\omega_d = 100$ meV, $\hbar\omega_0 = 100.125$ meV, $Q = 75$.

To demonstrate this principle, in this Letter we show how feedback due to the internal fields of a metallic disk driven at a frequency close to its natural dipole resonance (Fig. 1**a**) gives rise to multistability and spontaneous symmetry breaking. When excited, the resonance may produce rotating fields that modify the system's Bloch band Berry curvature (Fig. 1**b**). The resulting amplitude-dependent Berry flux splits the resonance for right- and left-handed polarizations. This feedback between field strength, field chirality, and Berry flux ultimately leads to *Berryogenesis*: the spontaneous appearance of a chiral circulating motion together with a non-vanishing Berry flux in a time-reversal symmetric system driven by a linearly polarized field (Fig. 1**c**).

The threshold driving amplitudes that are needed to induce Berryogenesis are modest, and can be achieved in current high quality graphene devices [7–9] with readily available terahertz to mid-infrared drives. While we use graphene for illustration due to its simplicity and favorability for near-term experiments, the mechanism we discuss is general and may apply to a wide variety of materials (e.g., transition metal dichalcogenides and multiband semimetals). The ease with which large plasmon-enhanced internal fields can be accessed in graphene [6, 9] makes it a natural platform for plasmonic non-equilibrium spontaneous symmetry breaking.

Berry flux generation — We now demonstrate how a nonvanishing Berry flux can be induced in a time-reversal-symmetric metal subjected to an off-resonant ac field. As a concrete example we consider electrons in graphene at finite doping, with Fermi energy $E_F > 0$.

Taking E_F as the natural energy scale, we express the Hamiltonian for electrons in the K valley of graphene as

$$\mathcal{H}_K = E_F\big[\tilde{\mathbf{k}} - \tilde{\mathbf{A}}(t)\big]\cdot\boldsymbol{\sigma}, \quad \tilde{\mathbf{A}}(t) = \frac{ev}{cE_F}\mathbf{A}(t), \qquad (1)$$

where v is graphene's Fermi velocity, c is the speed of light, $-e < 0$ is the electron charge, $\boldsymbol{\sigma} = (\sigma_x, \sigma_y)$ is a vector of Pauli matrices, and $\tilde{\mathbf{k}} = \mathbf{k}/k_F$ is the normalized 2D wave vector, with $\hbar v k_F = E_F$. The vector potential $\mathbf{A}(t)$ describes the (time-varying) electromagnetic (EM) field. Importantly, $\mathbf{A}(t)$ may arise both due to an externally applied driving field, and due to time-dependent internal fields of the system when it is driven out of equilibrium. The Hamiltonian $\mathcal{H}_{K'}$ for electrons in the K' valley is the same as that in Eq. (1), with $\sigma_y \to -\sigma_y$ in $\boldsymbol{\sigma}$.

For illustration we focus on a monochromatic field, $\mathbf{A}(t)$, oscillating at frequency ω. Crucially, we will consider off-resonant frequencies with $\hbar\omega < 2E_F$ such that absorptive transitions are prevented by Pauli blocking. In this situation, the main action of the time-varying $\mathbf{A}(t)$ in Eq. (1) is to dress/hybridize the wave functions in the conduction and valence bands of $\mathcal{H}_0$ [10]. Below it will be convenient to work in the basis of circularly polarized fields, $\mathbf{A}(t) = \frac{1}{2}(\mathbf{A}_L + \mathbf{A}_R)e^{-i\omega t} + c.c.$, where the left- and right-handed components are given by $\mathbf{A}_L = A_L(\hat{\mathbf{x}} + i\hat{\mathbf{y}})/\sqrt{2}$ and $\mathbf{A}_R = A_R(\hat{\mathbf{x}} - i\hat{\mathbf{y}})/\sqrt{2}$.

We analyze the induced Berry flux by studying the Floquet-Bloch band structure arising from Eq. (1) with the time-periodic field $\mathbf{A}(t)$ [see Methods]. Due to time-reversal symmetry (TRS), the time-averaged Berry flux $\bar{\mathcal{F}}$ associated with the Floquet Fermi sea must vanish for a linearly polarized field, i.e., for $|A_L| = |A_R|$. However, a chiral field with $|A_L| \neq |A_R|$ breaks TRS. In this case, the field-induced band hybridization manifests as a canting of the electronic pseudospins (Fig. 1**b**), which yields a finite Berry flux, $\mathcal{F} \neq 0$ [17, 19, 21–23].

In Fig. 2**a** we show the dc Berry flux induced by an off-resonant field, as a function of the (scaled) left- and right-hand circulating field amplitudes $\tilde{A}_L$ and $\tilde{A}_R$. In this

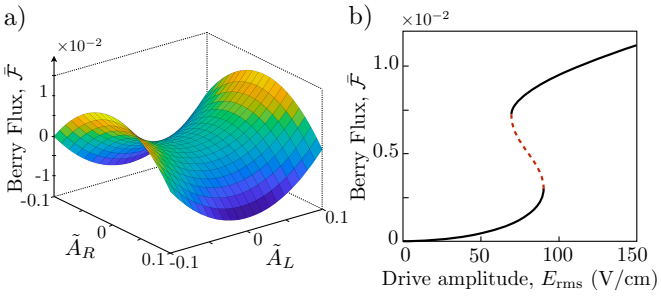

FIG. 2: Berry flux generation and non-linear plasmon dynamics. a) Time-averaged Berry flux induced by a harmonic drive with angular frequency ω_d and (dimensionless) left- and right-circular polarization amplitudes $\tilde{A}_L$ and $\tilde{A}_R$, respectively [see Eq. (1)]. In the off-resonant regime, the induced flux is approximately given by $\bar{\mathcal{F}} \approx \beta(|\tilde{A}_L|^2 - |\tilde{A}_R|^2)$, where $\beta \sim \mathcal{O}(1)$ depends on $\hbar\omega_d/E_F$. The surface shown is for $\hbar\omega/E_F = 0.625$. b) Steady state Berry flux for a graphene disk driven by a circularly polarized driving field. Stable and unstable steady states are indicated by black solid and red dashed lines, respectively. Parameters: $E_F = 160$ meV, $\hbar\omega_d = 100$ meV, $\hbar\omega_0 = 100.75$ meV, $Q = 100$.

regime, $\bar{\mathcal{F}}$ exhibits a characteristic saddle-like shape $\bar{\mathcal{F}} \approx \beta(|\tilde{A}_L|^2 - |\tilde{A}_R|^2)$, as may be anticipated by second-order perturbation theory. Here β is an $\mathcal{O}(1)$ dimensionless prefactor; for the parameters in graphene used in Fig. 2**a** we find $\beta \approx 2.3$. Berry flux generation thus provides a sensitive detector for TRS breaking, and as we discuss below, naturally couples with plasmonic dynamics.

Non-linear plasmon dynamics — When a plasmonic mode is excited near resonance, $\mathbf{A}(t)$ in Eq. (1) may easily be dominated by internal fields associated with the oscillating charge density in the system [5, 6]. Importantly, the plasmon resonance itself is sensitive to the development of Berry flux; this feedback provides the crucial source of plasmonic nonlinearity that we study.

To illustrate this phenomenon we consider the dipolar mode of a circular electronic disk (Fig. 1**a**). We describe the plasmon dynamics using center of mass (COM) coordinates for position, $\{\mathbf{r}(t)\} = \{x(t), y(t)\}$, and momentum, $\{\mathbf{p}(t)\} = \{p_x(t), p_y(t)\}$. Here $\{\cdot\}$ denotes an average over the electronic distribution function. The resulting plasmon equations of motion (derived from the kinetic equation [28–30]) are given by:

$$\frac{d\{\mathbf{r}\}}{dt} = \frac{\{\mathbf{p}\}}{m} - \frac{\mathcal{F}[\mathbf{E}_{\rm tot}(t)]}{\hbar n_0}\hat{\mathbf{z}}\times e\mathbf{E}_{\rm tot}(t),$$
$$\frac{d\{\mathbf{p}\}}{dt} = -m\omega_0^2\{\mathbf{r}\} - \gamma\{\mathbf{p}\} - e\mathbf{E}_{\rm drive}(t), \qquad (2)$$

where ω_0 is the angular frequency of the bare plasmon resonance of the disk (i.e., for $\mathcal{F} = 0$), m is the plasmon mass, n_0 is the electron density, and γ is the damping rate of the plasmon mode [36]. The fields $\mathbf{E}_{\rm tot}(t)$ and $\mathbf{E}_{\rm drive}(t) \sim e^{-i\omega_d t}$ are the total and the (monochromatic) driving electric fields, respectively. Here ω_d is the angular

frequency of the drive. Importantly, for $\mathcal{F} \neq 0$, the cross product in the first line of Eq. (2) couples the modes with linear polarizations along $\hat{\mathbf{x}}$ and $\hat{\mathbf{y}}$. The nonlinearity of the system arises due to the dependence of $\mathbf{E}_{\rm tot}$ on the plasmonic motion, $\{\mathbf{r}(t)\}$ (see below).

Within our mean-field approach, that focuses on the COM motion of the plasmon dipole, any spatial dependence of the internal and external fields is integrated out to obtain the effective electric field acting on the COM: $-e\mathbf{E}_{\rm tot}(t) = -e\mathbf{E}_{\rm drive}(t) - m\omega_0^2\{\mathbf{r}\}$, where $-m\omega_0^2\{\mathbf{r}\}$ is the restoring force acting on the COM. Close to resonance, the plasmonic internal field is enhanced by a factor $\omega_0/\gamma = 2Q$ relative to the driving field, where Q is the quality factor of the resonance. For large Q [7–9], the total electric field may thus be well approximated by $e\mathbf{E}_{\rm tot}(t) \approx m\omega_0^2\{\mathbf{r}(t)\}$; for simplicity, we make this replacement in the analysis below.

Our approach [Eq. (2)] is designed to capture the time-periodic *steady-state* motion of the system, where the Berry flux $\mathcal{F}$ is determined self-consistently from the (periodic) oscillating external and internal fields present in the steady-state. Transient dynamics, including fluctuations in the vicinity of the phase transition [31], are beyond the scope of this work. Noting that the time-averaged part of the Berry flux plays the most essential role in altering the character of the plasmon dynamics, below we replace $\mathcal{F}$ by its time-averaged value, $\bar{\mathcal{F}}$, in Eq. (2). This approximation preserves the crucial nonlinearity associated with the dependence of $\bar{\mathcal{F}}$ on $\{\mathbf{r}(t)\}$, and enables a detailed analytical treatment; see Methods for details of a fully self-consistent numerical solution.

We now solve for the steady-state plasmonic oscillations described by Eq. (2) with $\mathcal{F}$ replaced by $\bar{\mathcal{F}}$. Feedback due to self-generated Berry flux arises via the saddle-like dependence of $\bar{\mathcal{F}}$ on $\tilde{A}_L$ and $\tilde{A}_R$ (see Fig. 2**a**). To capture this interplay, we decompose the steady state motion in terms of right (+) and left (-) circulating amplitudes, $\mathcal{Z}_\pm^{(0)}$ (see Methods and **SI** [35]). We identify the internal field contribution to $\mathbf{A}(t)$ in Eq. (1) by using $\mathbf{E}_{\rm tot}(t) = -\frac{1}{c}\frac{\partial}{\partial t}\mathbf{A}(t)$, together with the replacement $e\mathbf{E}_{\rm tot}(t) \approx m\omega_0^2\{\mathbf{r}\}$. In this way we obtain the self-generated (dc) Berry flux:

$$\bar{\mathcal{F}} = f(|\mathcal{Z}_-^{(0)}|^2/l^2, |\mathcal{Z}_+^{(0)}|^2/l^2), \quad l^{-1} = \frac{vm\omega_0^2}{E_F\omega_d}, \qquad (3)$$

where f is the (dimensionless) saddle function of Fig. 2**a**, and l defines an intrinsic length scale of the system [35].

Transforming Eq. (2) to the circular polarization basis, and defining $\mathcal{E}^{\pm}_{\rm drive}(t) = \frac{1}{\sqrt{2}}[E^x_{\rm drive}(t) \pm iE^y_{\rm drive}(t)] = \mathcal{E}_\pm^{(0)}e^{-i\omega_d t}$, we find that the amplitudes $\mathcal{Z}_\pm^{(0)}$ are given by:

$$\mathcal{Z}_\pm^{(0)} = \frac{-e\mathcal{E}_\pm^{(0)}/m}{[-\omega_d^2 + \omega_0^2 \pm \kappa\bar{\mathcal{F}}\omega_d] - i\gamma[\omega_d \mp \kappa\bar{\mathcal{F}}]}, \qquad (4)$$

where $\kappa = m\omega_0^2/(\hbar n_0)$. Equation (4) demonstrates how a dc Berry flux $\bar{\mathcal{F}}$ modifies the disk's dipole resonance [30].

Importantly, because $\bar{\mathcal{F}}$ in Eq. (4) depends on $\mathcal{Z}_\pm^{(0)}$ via Eq. (3), the system may exhibit multistability. For demonstration, we first consider the simple case of a circularly polarized drive, $\mathcal{E}_+^{(0)} = 0$, $\mathcal{E}_-^{(0)} = E_{\rm rms}$. Here, the steady state motion captured by Eq. (4) is itself circularly polarized: there is no mixing between left and right hand polarizations. In Fig. 2**b** we show the corresponding solutions of Eq. (4), using the parametrized form $\bar{\mathcal{F}} = \beta(|\tilde{A}_L|^2 - |\tilde{A}_R|^2) = \beta l^{-2}(|\mathcal{Z}_-^{(0)}|^2 - |\mathcal{Z}_+^{(0)}|^2)$. We track the bistability via the induced (dc) Berry flux, $\bar{\mathcal{F}}$, as it provides a sensitive measure of the amplitude of circular motion. Note that for a circularly-polarized driving field in Eq. (1), the induced Berry flux $\mathcal{F}$ is in fact time-independent: $\mathcal{F}(t) = \bar{\mathcal{F}}$.

In the absence of driving, the graphene disk possesses zero Berry flux, $\mathcal{F} = 0$. As shown in Fig. 2**b**, as the amplitude of the circularly polarized drive is increased from zero, a finite Berry flux is generated. Strikingly, when the drive amplitude is strong enough, the induced Berry flux exhibits *bistability*: two distinct steady-state Berry fluxes [corresponding to two stable steady-state amplitudes for $\mathcal{Z}_-^{(0)}$ in Eq. (4)] may arise for the same drive amplitude. For even stronger driving, only the solution with a large self-generated contribution to the Berry flux remains.

Bistability arises from the fact that the (self-induced) Berry flux splits and shifts the plasmon resonances of the disk. Consider a weak external drive, with frequency ω_d slightly red-detuned from the bare resonance ω_0. The drive induces a small amplitude circular motion of the plasmon dipole, which correspondingly generates a small Berry flux, $\bar{\mathcal{F}}$. Due to the nonvanishing $\bar{\mathcal{F}}$, the resonance shifts downward, *toward* the frequency of the drive [37]. As the resonance approaches ω_d, the amplitude of response increases, thereby amplifying $\bar{\mathcal{F}}$ and bringing the drive even closer to resonance [38]. This feedback provides the mechanism for bistability.

Berryogenesis: spontaneous magnetization — We now turn our attention to the main phenomenon of interest: the spontaneous generation of Berry flux in a time-reversal symmetric driven system. The spontaneous TRS breaking is characterized by a magnetization order parameter: $\eta \equiv |\mathcal{Z}_+^{(0)}|^2 - |\mathcal{Z}_-^{(0)}|^2$. A non-zero value of η indicates the presence of an internal field exhibiting a net right ($\eta > 0$) or left ($\eta < 0$) handed rotation; as discussed above, such a rotating field induces a finite Berry flux. Once a finite $\mathcal{F}$ is present, the shifting of resonances helps to reinforce and amplify the circulating motion. This feedback is the driving force that enables *Berryogenesis* in time-reversal symmetric systems.

To illustrate spontaneous TRS breaking, we return to Eq. (4), with a *linearly polarized* drive $\mathcal{E}_+^{(0)} = \mathcal{E}_-^{(0)} = E_{\rm rms}$. For the simple parametrized saddle form considered above, the dc Berry flux is a function of η alone: $\bar{\mathcal{F}} = -\beta l^{-2}\,\eta$. Subtracting the expressions for $|\mathcal{Z}_-^{(0)}|^2$ and $|\mathcal{Z}_+^{(0)}|^2$ from Eq. (4), we obtain an algebraic relation

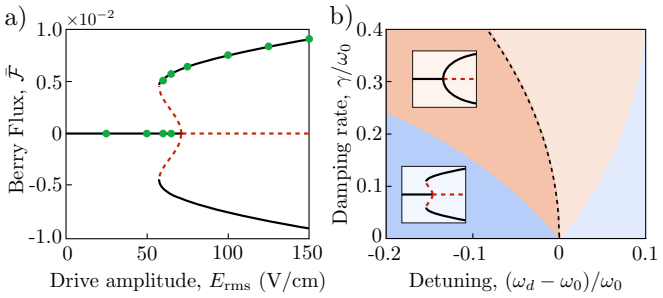

FIG. 3: Spontaneous magnetization in the presence of a time-reversal invariant, linearly-polarized drive. a) Stability diagram in the discontinuous transition regime. Stable (unstable) solutions of Eq. (5) are indicated by black solid (red dashed) lines. Green circles indicate self-consistent solutions to Eq. (2) in which the full time-dependence of $\mathcal{F}(t)$ is calculated from the self-induced Floquet band structure. Parameters: $E_F = 160$ meV, $\hbar\omega_d = 100$ meV, $\hbar\omega_0 = 100.5$ meV, $Q = 100$. b) The phase transition to the magnetized state can be either continuous (pink region) or discontinuous (blue region), depending on the detuning and damping rate. No instability occurs in the region to the right of the dashed line.

for the steady state magnetization:

$$\eta\left[1+4\nu\omega_d(\omega_d^2+\gamma^2-\omega_0^2)\frac{|eE_{\rm rms}/m|^2}{D_+D_-}\right]=0, \quad (5)$$

with $D_\pm=[\omega_0^2-\omega_d^2\mp\nu\omega_d\eta]^2+\gamma^2(\omega_d\pm\nu\eta)^2$ and $\nu=\kappa\beta/l^2$.

Equation (5) can be expressed as a fifth-order polynomial in η, and may exhibit several solutions (see Figs. 1**c** and 3**a**). For small amplitudes of the linearly-polarized drive, the system responds with linearly-polarized oscillations ($\eta = 0$). As the drive amplitude is increased, a bifurcation is encountered where the linearly polarized solution becomes unstable to fluctuations and the system spontaneously acquires a magnetization ($\eta \neq 0$) [39]. The appearance of such pitchfork bifurcations is consistent with symmetry considerations [32].

We confirm the validity of the results above, which were obtained by replacing $\mathcal{F}$ by $\bar{\mathcal{F}}$ in Eq. (2), by numerically obtaining self-consistent solutions of Eq. (2) including the full time dependence of $\mathcal{F}(t)$ [see Methods]. As shown in Fig. 3**a**, the time-averaged magnetization obtained from these simulations (green dots) agrees well with the results of our analytical treatment (solid lines).

Interestingly, the type of phase transition (discontinuous vs. continuous) is controlled by the detuning of the drive, $(\omega_d-\omega_0)/\omega_0$, and the damping rate, γ. The character of the transition can be straightforwardly extracted from the η dependence of the expression in brackets in Eq. (5), see **SI** [35]. As summarized in Fig. 3**b**, we find that: i) spontaneous magnetization may only occur for $(\omega_d^2+\gamma^2-\omega_0^2)<0$, and ii) for small detunings, discontinuous transitions are favored at low damping (high Q). Note that spontaneous symmetry breaking persists for $\gamma = 0$. Inspecting Eq. (5) and Fig. 3b for $\gamma = 0$, we see that in the absence of damping the transition occurs on the red detuned side of the resonance, and is always of discontinuous type ($B < 0$).

Discussion — The phenomena described above are enabled by strong internal plasmonic fields, which for a high quality resonance can exceed the driving field by several orders of magnitude. The threshold driving amplitude for Berryogenesis is therefore controlled by the plasmonic quality factor, along with other device parameters. For the high quality factors ($Q > 100$) recently achieved in graphene plasmonic devices [8], we expect Berryogenesis to be achievable at moderate driving powers of order 30 W/cm^2 at a frequency of $\sim$25 THz (see **SI** [35]).

Throughout this work we have focused on feedback arising from self-generated Berry flux. At high excitation amplitudes, nonlinear dissipation and other sources of nonlinearity may also arise. Crucially, we work at frequencies outside the particle-hole continuum, $\hbar\omega_d < 2E_F$, where both direct absorption from the drive (which leads to heating) and the decay of a single plasmon into a particle-hole pair is forbidden by Pauli exclusion. To suppress the nonlinear contributions to damping and heating, it is furthermore beneficial to work at lower frequencies where two- or three-photon processes are also blocked; for the simulations in this work we used $2E_F > 3\hbar\omega_d$, guaranteeing that the rates of these intrinsic dissipative processes are small throughout the parameter range we studied. Furthermore, we have checked that driving-induced anisotropies are also small throughout this regime, and are not expected to significantly affect the threshold for Berryogenesis (see **SI** [35]).

Berryogenesis is a "self-Floquet" process through which the collective motion of an electronic system causes it to reconstruct its own band structure, yielding dramatic effects including non-equilibrium spontaneous TRS breaking. Looking ahead, we anticipate that other types of non-equilibrium phase transitions [33], including complex spatiotemporal dynamics in extended systems [34], may be triggered by analogous feedback mechanisms. This work opens new prospects for exploiting the near-field compression of electromagnetic fields in metals to realize novel non-equilibrium phases of matter.

METHODS

Floquet band structure and Berry Flux

In the main text we describe how an (internal or external) ac electric field may modify the electronic spectrum and Bloch band Berry curvature of a metallic system. Here we describe how we calculate the time-dependent Berry flux induced by a monochromatic ac field. For each value of the crystal momentum **k**, we find two Floquet state solutions to the time-dependent Schrödinger

equation [25, 26]: $|\psi_{\mathbf{k}\alpha}(t)\rangle = e^{-i\varepsilon_{\mathbf{k}\alpha}t}|\Phi_{\mathbf{k}\alpha}(t)\rangle$, where $\alpha = \pm$ is the Floquet band index, $\varepsilon_{\mathbf{k}\alpha}$ is the corresponding quasienergy, and $|\Phi_{\mathbf{k}\alpha}(t)\rangle$ is a periodic function of time, with period $T = 2\pi/\omega$. Due to the off-resonant nature of the ac-field, states at the Fermi surface are only weakly modified; we assume that their populations map smoothly onto the Floquet states.

The periodic part of the Floquet eigenstate, $|\Phi_{\mathbf{k}\alpha}(t)\rangle$, typically involves frequency components at many harmonics of the drive frequency ω. As a result, the Berry connection $\mathcal{A}_{\mathbf{k}\alpha}(t) = \langle\Phi_{\mathbf{k}\alpha}(t)|i\nabla_{\mathbf{k}}|\Phi_{\mathbf{k}\alpha}(t)\rangle$, and ultimately the net Berry flux in the (dressed) conduction band [27], $\mathcal{F}(t) = \oint d\mathbf{k}\cdot\mathcal{A}_{\mathbf{k}+}(t)$, will be periodic functions of time. (Here the integral is taken around the Fermi surface.) In the analytical treatment in the main text we focus on the steady-state (dc) part of the induced Berry flux, $\bar{\mathcal{F}} = \frac{1}{T}\int_0^T dt\,\mathcal{F}(t)$, which captures the net breaking of time-reversal symmetry (TRS) and provides the driving force for *Berryogenesis*. Through fully self-consistent numerical simulations we show that including the ac part of $\mathcal{F}$ does not significantly alter our conclusions.

Self-consistent solutions of the steady state time evolution

In the main text, we provide a detailed analysis of the steady states of the nonlinear dynamics described by Eq. (2), under the approximation that the time-periodic Berry flux $\mathcal{F}(t)$ is replaced by its time-averaged (dc) part $\bar{\mathcal{F}}$. From a physical point of view, this approximation is motivated by the fact that it is the dc part of $\mathcal{F}$ that signifies a net breaking of TRS, and which we expect to be responsible for the instability towards a magnetized state. From a technical point of view, this approximation introduces a vast simplification: working in a complex representation with $\mathbf{E}_{\rm drive}(t) = \mathbf{E}^{(0)}_{\rm drive}\,e^{-i\omega_d t}$, by suppressing the time-dependent harmonics in $\mathcal{F}$, we ensure that Eq. (2) supports solutions where $\mathbf{r}(t) = \mathbf{r}^{(0)}e^{-i\omega_d t}$ and $\mathbf{p}(t) = \mathbf{p}^{(0)}e^{-i\omega_d t}$ exhibit purely monochromatic oscillations. (Note that the physical solutions are given by the real parts of these quantities.) This simplification allows us to extract the time dependence $\sim e^{-i\omega_d t}$ from all variables, and solve a (nonlinear) algebraic equation for the steady state amplitudes of the left- and right- circulating components of $\mathbf{r}(t)$, $\mathcal{Z}^{(0)}_{\pm} = \frac{1}{\sqrt{2}}[x^{(0)} \pm iy^{(0)}]$. These solutions are given in Eq. (4) of the main text.

To support our conclusions and to demonstrate that the time-dependent harmonics in $\mathcal{F}(t)$ do not significantly change the behavior of the system, we also performed self-consistent numerical simulations of the full equations of motion, Eq. (2). The simulations were performed as follows:

1. We first initialize the system with values of position and momentum, $\mathbf{r}(0)$ and $\mathbf{p}(0)$, as well as an initial guess for the Berry flux $\mathcal{F}$. The Berry flux $\mathcal{F}$ is specified by its dc part $\bar{\mathcal{F}}$ and a list of up to n harmonics, $\mathcal{F}_1 \ldots \mathcal{F}_n$, such that $\mathcal{F}(t) = \bar{\mathcal{F}} + (\mathcal{F}_1 e^{-i\omega_d t} + \ldots \mathcal{F}_n e^{-in\omega_d t} + \text{c.c.})$. The value of n is taken large enough to ensure convergence.

2. Next we numerically solve Eq. (2) with the supplied form of $\mathcal{F}(t)$ for a large number of periods of the drive (typically of order 100), such that the system reaches a time-periodic steady state.

3. From the last several periods of evolution, we extract the left- and right-handed components of the motion via $\mathcal{Z}_{\pm}(t) = (x \pm iy)/\sqrt{2}$. From the Fourier transform of $\mathcal{Z}_{\pm}(t)$, we extract the values at its peaks centered around frequencies ω_d, $2\omega_d$, etc.

4. We use the harmonics extracted from $\mathcal{Z}_{\pm}(t)$ to construct the time-periodic internal electric field and associated vector potential produced by the motion via $e\mathbf{E}_{\rm int} = m\omega_0^2\mathbf{r}$ and $\mathbf{E}_{\rm int} = -\frac{1}{c}\frac{\partial}{\partial t}\mathbf{A}_{\rm int}$.

5. We numerically compute the Floquet band structure of the system using the total time-periodic field $\mathbf{A}_{\rm tot} = \mathbf{A}_{\rm drive} + \mathbf{A}_{\rm int}$. We obtain a new time-periodic Berry flux $\mathcal{F}(t)$ by integrating the Berry connection $\mathcal{A}_{\mathbf{k}+}(t) = \langle\Phi_{\mathbf{k}+}(t)|i\nabla_{\mathbf{k}}|\Phi_{\mathbf{k}+}(t)\rangle$ around the Fermi surface, $\mathcal{F}(t) = \oint d\mathbf{k}\cdot\mathcal{A}_{\mathbf{k}+}(t)$. Here $|\Phi_{\mathbf{k}+}(t)\rangle$ is the time-periodic part of the Floquet state at crystal momentum $\mathbf{k}$ in the upper (+) Floquet band, derived from the original conduction band on the non-driven system.

6. Finally we return to step 1 and initialize the solver for Eq. (2) with the final position and momentum of the previous iteration, and a new guess for $\mathcal{F}(t)$. This procedure is iterated until the Berry flux $\mathcal{F}(t)$ produced by the motion agrees with form that was used to compute it (i.e., until the change in $\mathcal{F}(t)$ from one iteration to the next falls below a convergence threshold).

To improve stability of the code, we introduce an interpolating factor ζ such that the initial guess for the Berry flux for iteration $i+1$, $\mathcal{F}^{(i+1)}$, is computed by interpolating between its value on iteration i and the new value computed in step 5 above: $\mathcal{F}_n^{(i+1)} = (1-\zeta)\mathcal{F}_n^{(i)} + \zeta\mathcal{F}_n$. Here $\mathcal{F}_n$ is the n-th harmonic extracted from the Fourier transform of $\mathcal{F}(t)$ computed in step 5 above. In the simulations shown we used $\zeta = 0.3$. For each value of the driving amplitude we obtained convergence of all harmonics in $\mathcal{F}$ to better than 1 part in 10^6.

We observe that, throughout the parameter regime studied, the higher harmonics of $\mathcal{F}$ decay very quickly with the order of the harmonic. (As a typical order of magnitude, we observe $\mathcal{F}_1/\bar{\mathcal{F}} \sim 10^{-3}$.) Therefore we obtain rapid convergence with respect to the number of

harmonics retained (in the simulations we keep the track the values of the first 5 harmonics of $\mathcal{F}$).

The procedure above was used to compute the green points shown in Fig. 3**a**. The good agreement with the solid curves confirms that the validity of our analytical treatment based on the dc part of $\mathcal{F}$.

Data availability — The data that support the plots within this paper and other findings of this study are available from the corresponding author upon reasonable request.

Acknowledgements — We thank D. Huse, M. Kats, M. Katsnelson, L. Levitov, R. Nandkishore, L. Radzihovsky, and G. Refael for helpful discussions. M.S.R. gratefully acknowledges the support of the European Research Council (ERC) under the European Union Horizon 2020 Research and Innovation Programme (Grant Agreement No. 678862), and the Villum Foundation. J.C.W.S. gratefully acknowledges the support of the Singapore National Research Foundation (NRF) under NRF fellowship award NRF-NRFF2016-05, and a start-up grant from the Nanyang Technological University.

* Electronic address: rudner@nbi.ku.dk
† Electronic address: justinsong@ntu.edu.sg

[1] P. M. Chaikin and Tom C. Lubensky, *Principles of condensed matter physics* Vol. 1. Cambridge: Cambridge university press, (1995).
[2] H. Haken, "Cooperative phenomena in systems far from thermal equilibrium and in nonphysical systems," Rev. Mod. Phys. **47**, 67 (1975).
[3] J. Goldstone, A. Salam, S. Weinberg, "Broken symmetries" Phys. Rev **127**, 965 (1962).
[4] D. N. Basov, M. M. Fogler, F. J. García de Abajo, "Polaritons in van der Waals materials" Science **354**, 6309 (2016).
[5] H. A. Atwater and A. Polman, "Plasmonics for improved photovoltaic devices," Nature Materials **9**, 205 (2010).
[6] F. H. L. Koppens, D. E. Chang, and F. Javier Garcia de Abajo, "Graphene plasmonics: a platform for strong light-matter interactions," Nano letters **11** 3370 (2011).
[7] A. Woessner, *et al.*, "Highly confined low-loss plasmons in graphene-boron nitride heterostructures," Nature Materials **14**, 421 (2015).
[8] G. X. Ni, A. S. McLeod, Z. Sun, L. Wang, L. Xiong, K. W. Post, S. S. Sunku, B. Y. Jiang, J. Hone, C. R. Dean, M. M. Fogler, and D. M. Basov, "Fundamental limits to graphene plasmonics," Nature **557**, 530 (2018).
[9] D. A. Iranzo, *et al.*, "Probing the ultimate plasmon confinement limits with a van der Waals heterostructure," Science **360**, 291 (2018).
[10] W. Yao, A. H MacDonald, and Q. Niu, "Optical control of topological quantum transport in semiconductors," Phys. Rev. Lett. **99**, 047401 (2007).
[11] E. J. Sie, J. W. McIver, Y.-H. Lee, L. Fu, J. Kong, and N. Gedik, "Valley-selective optical Stark effect in monolayer WS_2," Nature Materials **14**, 290 (2015).
[12] D. N. Basov, R. D. Averitt, and D. Hsieh, "Towards properties on demand in quantum materials," Nature Materials **16**, 1077 (2017).
[13] D. Fausti, R. I. Tobey, N. Dean, S. Kaiser, A. Dienst, M. C. Hoffmann, S. Pyon, T. Takayama, H. Takagi, and A. Cavalleri, "Light-induced superconductivity in a stripe-ordered cuprate," Science **331**, 189 (2011).
[14] R. Mankowsky, *et al.*, "Nonlinear lattice dynamics as a basis for enhanced superconductivity in $YBa_2Cu_3O_{6.5}$," Nature **516**, 71 (2014).
[15] M. Mitrano, *et al.*, "Possible light-induced superconductivity in K_3C_{60} at high temperature," Nature **530**, 461 (2016).
[16] Y. H. Wang, H. Steinberg, P. Jarillo-Herrero, and N. Gedik, "Observation of Floquet-Bloch states on the surface of a topological insulator," Science **342**, 453 (2013).
[17] T. Oka and H. Aoki, "Photovoltaic Hall effect in graphene," Phys. Rev. B **79**, 081406 (2009).
[18] T. Kitagawa, E. Berg, M. Rudner, and E. Demler, "Topological characterization of periodically driven quantum systems," Phys. Rev. B **82**, 235114 (2010).
[19] T. Kitagawa, T. Oka, A. Brataas, L. Fu, and E. Demler, "Transport properties of nonequilibrium systems under the application of light: Photoinduced quantum Hall insulators without Landau levels," Phys. Rev. B **84**, 235108 (2011).
[20] N. H. Lindner, G. Refael, and V. Galitski, "Floquet topological insulator in semiconductor quantum wells," Nature Physics **7**, 490 (2011).
[21] Z. Gu, H. A. Fertig, D. P. Arovas, and A. Auerbach, "Floquet spectrum and transport through an irradiated graphene ribbon," Phys. Rev. Lett. **107**, 216601 (2011).
[22] G. Usaj, P. M. Perez-Piskunow, L. E. F. Foa Torres, and C. A. Balseiro, "Irradiated graphene as a tunable Floquet topological insulator," Phys. Rev. B **90**, 115423 (2014).
[23] D. Yudin, O. Eriksson, and M. I. Katsnelson, "Dynamics of quasiparticles in graphene under intense circularly polarized light," Phys. Rev. B **91**, 075419 (2015).
[24] J. Cayssol , B. Dora, F. Simon, and R. Moessner, "Floquet topological insulators," Phys. Status Solidi RRL, **7**, 101 (2013).
[25] J. H. Shirley, "Solution of the Schrodinger Equation with a Hamiltonian Periodic in Time," Phys. Rev. **138**, B979 (1965).
[26] H. Sambe, "Steady States and Quasienergies of a Quantum Mechanical System in an Oscillating Field," Phys. Rev. A **7**, 2203 (1973).
[27] F. D. M. Haldane, "Berry curvature on the Fermi surface: anomalous Hall effect as a topological Fermi-liquid property." Phys. Rev. Lett. **93**, 206602 (2004).
[28] D. T. Son and N. Yamamoto, "Berry Curvature, Triangle Anomalies, and the Chiral Magnetic Effect in Fermi Liquids," Phys. Rev. Lett. **109**, 181602 (2012).
[29] D. T. Son, and B. Z. Spivak, "Chiral anomaly and classical negative magnetoresistance of Weyl metals," Phys. Rev. B **88**, 104412 (2013).
[30] J. C. W. Song and M. S. Rudner, "Chiral plasmons without magnetic field," Proceedings of the National Academy of Sciences **113**, 4658 (2016).
[31] M. I. Dykman and M. A. Krivoglaz, "Fluctuations in nonlinear systems near bifurcations corresponding to the appearance of new stable states," Physica **104 A**, 480 (1980).
[32] M. I. Dykman, "Theory of optical polarization bistabil-

ity", Sov. Phys. JETP **64**, 927 (1986).
[33] M. S. Foster, V. Gurarie, M. Dzero, E. A. Yuzbashyan, "Quench-Induced Floquet Topological p-Wave Superfluids", Phys. Rev. Lett. **113**, 076403 (2014).
[34] J. Alicea, L. Balents, M. P. A. Fisher, A. Paramekanti, and L. Radzihovsky, "Transition to zero resistance in a two-dimensional electron gas driven with microwaves," Phys. Rev. B **71**, 235322 (2005).
[35] See **Supplementary Information** for a discussion of self-induced Berry flux and its relation to the oscillating total electric field, an estimate of the critical field strength, and a discussion EM-induced dispersion anisotropy.
[36] We include γ in the equation of motion to account for the plasmon damping that inevitably arises in real devices. However, dissipation is *not* essential for multistability or spontaneous symmetry breaking in this system.
[37] The direction of the shift is controlled by microscopic parameters of the system; for a right- or left-handed drive the sign is the same, but for hole-doped graphene with $E_F < 0$, for example, the sign would be reversed.
[38] For a blue-detuned drive, *negative feedback* is obtained as the resonance is pushed away from the drive frequency. In this case, no multistability is expected.
[39] The handedness of the steady-state motion is chosen *spontaneously*, much as a ferromagnet spontaneously chooses a magnetic orientation when cooled below its Curie temperature.

SUPPLEMENTARY INFORMATION FOR "SELF-INDUCED BERRY FLUX AND SPONTANEOUS NON-EQUILIBRIUM MAGNETISM"

SELF-INDUCED BERRY FLUX

In the following we discuss how internal rotating electric fields, captured by a circulating plasmon center of mass (COM) coordinate $\mathcal{Z}_\pm^{(0)} = \frac{1}{\sqrt{2}}[x^{(0)} \pm iy^{(0)}]$, directly generates a Berry flux of the electrons. To do this, we first recall that oscillating electric fields $\mathbf{E}(t) = \mathbf{E}^{(0)}\, e^{-i\omega_d t}$ can be expressed in terms of a time varying vector potential: $\mathbf{A}(t) = \mathbf{A}^{(0)}\, e^{-i\omega_d t}$, where

$$\mathbf{E}^{(0)} = (i\omega/c)\mathbf{A}^{(0)}. \tag{S-1}$$

As in the main text, we use the circular polarization basis to describe the vector potential fields: $\mathbf{A}(t) = \frac{1}{2}(\mathbf{A}_L + \mathbf{A}_R)e^{-i\omega t} + c.c.$, where the left- and right-handed components are given by $\mathbf{A}_L = A_L(\hat{\mathbf{x}} + i\hat{\mathbf{y}})/\sqrt{2}$ and $\mathbf{A}_R = A_R(\hat{\mathbf{x}} - i\hat{\mathbf{y}})/\sqrt{2}$.

Circularly polarized fields modify the system's band structure and electronic wave functions. In this way the Fermi sea may acquire a finite (dc) Berry flux:

$$\bar{\mathcal{F}} = f(|\tilde{A}_L|^2, |\tilde{A}_R|^2), \quad \tilde{\mathbf{A}}_{L,R} = \frac{ev}{cE_F}\mathbf{A}_{L,R}, \tag{S-2}$$

where f is the (dimensionless) saddle shown in Fig. 2**a**.

Crucially, the fields in Eq. (S-2) consist of both external driving fields as well as *internal* plasmonic fields. Within our mean-field approach, the total electric field on the COM can be expressed $-e\mathbf{E}_{\rm tot}(t) = -e\mathbf{E}_{\rm drive}(t) - m\omega_0^2\{\mathbf{r}\}$, where $-m\omega_0^2\{\mathbf{r}\}$ is precisely the restoring force acting on the COM. When driven close to resonance, the plasmonic internal field is dramatically enhanced by a factor $\omega_0/\gamma = 2Q$ relative to the driving field, where Q is the quality factor of the resonance. Since Q can be large in high quality graphene disks, the total electric field can be dominated by internal fields with total electric fields well approximated by $e\mathbf{E}_{\rm tot}(t) \approx m\omega_0^2\{\mathbf{r}(t)\}$.

Using Eq. (S-1) above and taking $e\mathbf{E}_{\rm tot}(t) \approx m\omega_0^2\{\mathbf{r}(t)\}$, we can rewrite $\tilde{A}_{L,R}$ in terms of the plasmon COM coordinates $\mathcal{Z}_\pm^{(0)}$. The conversion between the dimensionless (total) vector potential $\tilde{A}_{L,R}$ and the coordinate $\mathcal{Z}_\pm^{(0)}$ is given by the characteristic length $l = E_F\omega_d/(vm\omega_0^2)$ which naturally emerges from the definition of $\tilde{\mathbf{A}}_{L,R}$ in Eq. (S-2), together with Eq. (S-1) and $e\mathbf{E}_{\rm tot}(t) \approx m\omega_0^2\{\mathbf{r}(t)\}$. Re-writing $\tilde{A}_{L,R} \to \mathcal{Z}_\pm^{(0)}/l$ (with $L \to -$ and $R \to +$) in Eq. (S-2) gives Eq. (3) of the main text.

CONTINUOUS *VS.* DISCONTINUOUS TRANSITION

As noted in the main text, the phase transition to the state with spontaneous non-equilibrium magnetization may occur either discontinuously as a function of driving amplitude (as in a first order phase transition), or continuously (akin to a second order phase transition). The character of the transition follows from the η-dependence of the expression in brackets in Eq. (5). For fixed parameters, the zeros of this expression (as a function of η) determine the steady state values of magnetization that can be supported by the system.

As a first step in characterizing the nature of the transition, we note that D_+D_- in Eq. (5) is positive for all η; this must be so, as D_+ and D_- are the squared absolute values of the denominators appearing in Eq. (4). Consequently, for $\nu > 0$, nontrivial zeros of the term in brackets in Eq. (5), and hence spontaneous magnetization, may only occur for $(\omega_d^2 + \gamma^2 - \omega_0^2) < 0$, i.e., to the left of the shaded region in Fig. 3**b**.

The character of the transition (continuous *vs.* discontinuous) is controlled by the sign of the quadratic term in η in D_+D_-. This can be seen by writing out $D_+D_- = A + B\eta^2 + C\eta^4$. Here A, B, and C are coefficients that depend on damping and detuning, with $A, C > 0$:

$$\begin{aligned} A &= [(\omega_0^2 - \omega_d^2)^2 + \gamma^2\omega_d^2]^2 \\ C &= \nu^4(\gamma^2 + \omega_d^2)^2. \end{aligned} \tag{S-3}$$

The form of B is straightforward to obtain from the explicit expressions for D_+ and D_- given in the main text; the result is long and not illuminating, so we do not write it out in full here. For $B > 0$ (pink region, Fig. 3**b**), $(D_+D_-)^{-1}$ decreases monotonically as a function of η^2. When $E_{\rm rms}$ is small, the second term in the brackets in Eq. (5) is less than one for all η, and no nontrivial solutions are found. Above the critical value of $E_{\rm rms}$, a new branch of solutions emerges with η growing continuously from zero. For $B < 0$ (blue region, Fig. 3**b**), $(D_+D_-)^{-1}$ is non-monotonic, first increasing for small η, then decreasing for large η. Here, as $E_{\rm rms}$ is increased from zero, nontrivial solutions first appear at finite η^2 [corresponding to the maximum of $(D_+D_-)^{-1}$], and we obtain a discontinuous transition as in Fig. 3**a**.

ESTIMATE FOR CRITICAL FIELD STRENGTHS

In the following, we provide an estimate of the critical driving amplitudes required to achieve spontaneous out-of-equilibrium plasmonic magnetism. As an illustration, we will focus on the parameter regime where $B > 0$ in Eq. (5) of the main text. In this regime, the solutions of Eq. (5) exhibit a continuous phase transition. In particular, non-trivial zeros of the bracketed expression in

Eq. (5) appear for $E_{\rm rms} > E^*_{\rm rms}$, where $E^*_{\rm rms}$ is the critical drive amplitude above which non-trivial solutions for η appear:

$$|eE^*_{\rm rms}|^2 = m^2 \frac{\left[(\omega_0^2-\omega_d^2)^2+\gamma^2\omega_d^2\right]^2}{4\nu\omega_d(\omega_d^2-\omega_0^2+\gamma^2)} \approx \frac{m^2\omega_0^5}{4\nu}\cdot\frac{1}{4Q^2}. \tag{S-4}$$

As a demonstration, in the second (approximate) equality we have set $\omega_d = \omega_0$, and used $\omega_0/\gamma = 2Q$ to express the result in terms of the quality factor. From the main text, recall that

$$\nu = \beta\kappa/l^2 = \beta\frac{m^3v^2\omega_0^6}{\hbar n_0 E_F^2\omega_d^2}. \tag{S-5}$$

Setting $\omega_d = \omega_0 = (2\pi e^2 n_0|\mathbf{q}|/m)^{1/2}$ and taking $|\mathbf{q}| = 1/d$, where d is the diameter of the disk we estimate the critical field to be:

$$|E^*_{\rm rms}| = 1.57{\times}10^2 \frac{(E_F[\text{eV}]/0.1)^{7/4}}{\beta^{1/2}\times(Q/100)\times(d[\mu\text{m}]/0.1)^{1/4}}[\text{V/cm}]. \tag{S-6}$$

In obtaining the above estimate we have noted that, for graphene, the plasmon mass can be written as $m = E_F/v^2$, with $v = 10^8$ cm/s, and we have included flavor degeneracy for 4 valleys/spins when calculating the density. Recently, quality factors for plasmons exceeding 100 have been realized, enabling even lower critical fields.

The corresponding incident power required to induce the phase transition can be obtained by recalling (in SI units) $P_{\rm incident} = \varepsilon_0 c|E_{\rm rms}|^2$, where ε_0 is the permittivity of free space. Taking $E^*_{\rm rms} \sim 100$ V/cm as a rough order of magnitude estimate, we obtain a modest steady-state incident power of $P^*_{\rm incident} \sim 26\,\text{W/cm}^2$.

INDUCED ANISOTROPIC DRUDE WEIGHT

In the main text we focused on the nonlinearity that arises due to self-induced Berry flux. In addition to the reconstruction of electronic wave functions that gives rise to the Berry flux, ac fields also modify the electronic dispersion. In particular, a linearly polarized ac field, which breaks the rotational symmetry of the system, generically introduces anisotropy in the dispersion. Such anisotropy in principle competes with spontaneous magnetization, as it favors a splitting of the plasmonic dipole resonance in the linear polarization basis (in contrast to magnetization, which is associated with circularly/elliptically polarized motion). Below we estimate the anisotropy of the Drude weight (plasmon mass) induced by a linearly-polarized ac electric field. We show that the induced anisotropy is small (of order 10^{-4}) in the regime studied, and therefore should not qualitatively affect our results.

To estimate the induced anisotropy of the Drude weight, we consider a linearly polarized field $A_x\cos(\omega t)\,\hat{\mathbf{x}} = \frac{1}{2}A_x(e^{i\omega t}+e^{-i\omega t})\hat{\mathbf{x}}$; note that for circularly polarized fields, no linear anisotropy develops. Using Eq. (1) of the main text, and transforming to the "extended space" Fourier representation in which the Fourier harmonics $\{|n\rangle\}$ are treated as an auxiliary degree of freedom, the light-matter interaction is described via: $\mathcal{H}_{\rm int} = \hat{V}\otimes\sum_n[|n+1\rangle\langle n| + |n-1\rangle\langle n|]$, where

$$\hat{V} = -\frac{E_F\tilde{A}_x}{2}\sigma_x. \tag{S-7}$$

The eigenvalues of the Hamiltonian in the extended space representation are the quasienergies of the associated Floquet states. Anisotropy in the Drude weight arises from EM field induced changes to the group velocity, different in the x and y directions, which in turn can be obtained from changes to the (quasi)-energy dispersion at the Fermi level.

The lowest order EM-field induced changes to the energy occur at second order, so that $\varepsilon_{\mathbf{k}} = \varepsilon^{(0)}_{\mathbf{k}} + \varepsilon^{(2)}_{\mathbf{k}}$. Focusing on the case where the Fermi level is in the conduction band, the unperturbed energy is $\varepsilon^{(0)}_{\mathbf{k}} = v|\mathbf{k}|$, and the second-order correction is:

$$\varepsilon^{(2)}_{\mathbf{k}} = |\langle\mathbf{k},-|\hat{V}|\mathbf{k},+\rangle|^2\left(\frac{1}{2\varepsilon^{(0)}_{\mathbf{k}}+\hbar\omega}+\frac{1}{2\varepsilon^{(0)}_{\mathbf{k}}-\hbar\omega}\right), \tag{S-8}$$

where $|\mathbf{k},\pm\rangle$ are the unperturbed electronic states in the conduction and valence bands respectively, and $\hbar\omega$ is the energy of the absorbed/emitted photon. The first term in Eq. (S-8) arises from the virtual absorption of a photon accompanied by an electronic transition to a valence band state, followed by photon emission and a transition back to the conduction band; the second term occurs for a similar process, where the system emits a photon while making the (virtual) transition from the conduction to the valence band. We note that there are two additional second order processes where photons are virtually absorbed/emitted without an accompanying electronic transition to the valence band. The corresponding terms in the energy shift have equal magnitude but opposite sign, and therefore cancel and do not contribute to the total $\varepsilon^{(2)}_{\mathbf{k}}$.

Using $\langle\mathbf{k},-|\sigma_x|\mathbf{k},+\rangle = i\sin 2\phi$, where $\tan\phi = k_y/k_x$, we have:

$$\varepsilon^{(2)}_{\mathbf{k}} = \frac{E_F^2|\tilde{A}_x|^2\varepsilon^{(0)}_{\mathbf{k}}}{(2\varepsilon^{(0)}_{\mathbf{k}})^2-(\hbar\omega)^2}\left[1-\frac{1}{|\mathbf{k}|^2}(k_x^2-k_y^2)\right]. \tag{S-9}$$

Here we used the identity $\sin^2 2\phi = 1-\cos^2 2\phi = 1-(\cos^2\phi-\sin^2\phi)$. To find the change to the Drude weight, we use Eq. (S-9) to fit the perturbed energies $\varepsilon_{\mathbf{k}} = \varepsilon^{(0)}_{\mathbf{k}} + \varepsilon^{(2)}_{\mathbf{k}}$ to the anisotropic Dirac dispersion

$$\begin{aligned}\varepsilon_{\mathbf{k}} &= U+\hbar\sqrt{(v-\delta v)^2k_x^2+(v+\delta v)^2k_y^2}\\ &= U+\varepsilon^{(0)}_{\mathbf{k}}-\varepsilon^{(0)}_{\mathbf{k}}\tfrac{\delta v}{v|\mathbf{k}|^2}(k_x^2-k_y^2)+\mathcal{O}(p^4),\end{aligned} \tag{S-10}$$

where U is a constant energy offset. Comparing the coefficient of the $k_x^2 - k_y^2$ term in Eq. (S-10) with Eq. (S-9) above, we obtain the velocity anisotropy as

$$\frac{\delta v}{v} = \frac{E_F^2 |\tilde{A}_x|^2}{(2\varepsilon_{\mathbf{k}}^{(0)})^2 - (\hbar\omega)^2} \approx 4.4 \times 10^{-4}. \tag{S-11}$$

In the last (approximate) equality we have made an estimate using $\varepsilon_{\mathbf{k}}^{(0)} \approx E_F = 160$ meV and $\hbar\omega = 100$ meV, as used for the figures in the main text, and have also used $|\tilde{A}_x| = ev\mathcal{E}_{\text{total}}/(\omega E_F) \approx 0.04$. For this last estimate, we used $\mathcal{E}_{\text{total}} = 10^4$ V/cm for the total field (external drive + plasmonic internal) close to the phase transition, see section above. Note that the small value of $\tilde{A}$ that we find indicates that the changes/boost to the Fermi sea as the electron liquid moves is small as compared with the Fermi surface size. We also note that the k-independent term in Eq. (S-9) can be absorbed into the energy offset term U with no changes to the velocity.

Since the Drude weight $D_{ij} = e^2 \sum_{\mathbf{k}} v_i(\mathbf{k}) v_j(\mathbf{k}) \delta(\varepsilon_{\mathbf{k}} - E_F)$ scales as the square of the velocity at the Fermi surface, we estimate that the EM-induced anisotropy to the Drude weight (along x or y directions) is $2\delta v/v \approx 9 \times 10^{-4}$ for the regime described above in Eq. (S-11). Drude weight anisotropy can be directly included in the equations of motion in Eq. (2) of the main text as a direction-dependent plasmon mass. We have numerically checked that incorporating anisotropy in the Drude weight of order 1% does not change the qualitative picture of our results, and only introduces modest quantitative changes to the threshold driving amplitude and induced Berry flux. As a result, given that the induced anisotropy is expected to be an order of magnitude smaller, we conclude that EM-induced anisotropies do not adversely affect the realization of the non-equilibrium TRS breaking phase transition we discuss in the main text.